Research Square

Preprints are preliminary reports that have not undergone peer review.
They should not be considered conclusive, used to inform clinical practice,
or referenced by the media as validated information.

Quantifying the Relative Contributions of Marine Air Penetration and Agricultural Irrigation to Planetary Boundary-Layer Development in California's Central Valley

Kuan-Yun (Grace) Wang
University of California, Davis
Shu-Hua Chen
shachen@ucdavis.edu

University of California, Davis
Cameron Schmitt
University of California, Davis
Yang Yu
University of California, Davis
Kosana Suvočarev
University of California, Davis
Ian Flynn McDonald
University of California, Davis
Xue-Meng Chen
California Air Resources Board
PingKuan Di
California Air Resources Board
Karry Liu
California Air Resources Board
Ying-Kuang Hsu
California Air Resources Board
Ranga Rajan Thiruvenkatachari
California Air Resources Board
Jeremy Avise
California Air Resources Board

Article

Keywords: Atmospheric Boundary Layer, California’s Central Valley, Irrigation, Marine Air Penetration

Posted Date: November 20th, 2026

DOI: https://doi.org/10.21203/rs.3.rs-11570414/v1

License: This work is licensed under a Creative Commons Attribution 4.0 International License.
Read Full License

Additional Declarations: No competing interests reported.

Quantifying the Relative Contributions of Marine Air Penetration and Agricultural Irrigation to Planetary Boundary-Layer Development in California's Central Valley

Kuan-Yun (Grace) Wang[1] · Shu-Hua Chen[1] · Cameron Schmitt[1,2] · Yang Yu[1,3], Kosana Suvočarev[1], Ian Flynn McDonald[1], Xue-Meng Chen[4], PingKuan Di[4], Karry Liu[4], Ying-Kuang Hsu[4], Ranga Rajan Thiruvenkatachari[5], Jeremy Avise[4]

Received: DD Month YEAR/ Accepted: DD Month YEAR/ Published online: DD Month YEAR
© Springer Science + Business Media B. V.

Abstract

Summertime planetary boundary-layer height (PBLH) across California's Central Valley (CV) is modulated by both agricultural irrigation and marine air penetration (MAP), with distinct regional patterns. Previous studies have examined these effects separately, using numerical models for irrigation and observational or reanalysis data for MAP. This study uses numerical modeling to quantify the relative contributions of irrigation versus MAP on PBLH changes across the CV during 21–27 July 2022 and to investigate the underlying mechanisms. Four experiments are conducted with the combinations of with (WIR) and without (WoIR) agricultural irrigation, and with and without MAP. The MAP effect is removed by filling mountain gaps to a minimum of 700 m. Compared with WoIR, the cooler surface temperature (i.e., lower sensible heat flux) due to stronger evapotranspiration in WIR weakens dry convection, resulting in a decrease of PBLH in the northern (southern) CV by 0.5–1.5 km (0.5–1 km) where the irrigation rate is high. In contrast, the MAP effect stabilizes the lower atmosphere by advecting cold air to the lower

✉ Corresponding Author: Shu-Hua Chen. Email: shachen@ucdavis.edu

[1] Department of Land, Air and Water Resources, University of California, Davis, CA 95616, United States.

[2] Department of Civil and Environmental Engineering, University of California, Irvine CA, 92697, United States

[3] Department of Physical Oceanography, Woods Hole Oceanographic Institute, Woods Hole MA, 02543

[4] Air Quality Planning & Science Division, California Air Resources Board, CA 95814, USA

[5] Monitoring Laboratory Division, California Air Resources Board, CA 95814, USA

atmosphere and reduces PBLH across the CV by roughly 0.5–1 km. The stabilization layer by MAP in the northern CV is shallower than that in the southern CV. Overall, between the two effects, irrigation contributes more than 50% of the total PBLH reduction in the northern and southern CV, whereas MAP contributes to ~100% of the total PBLH reduction in the central CV, decaying away from the MAP sources.

Keywords Atmospheric Boundary Layer · California's Central Valley · Irrigation · Marine Air Penetration

1 Introduction

The planetary boundary layer (PBL), the lowest well-mixed layer of the troposphere, plays a critical role in air quality, the Earth's energy budget, weather, and climate. Regarding air quality, because pollutants are emitted primarily from the surface and are trapped within the PBL, their concentrations depend strongly on the PBL depth and the wind structure within it (Berman et al. 1999; Trousdell et al. 2016; Pan and Faloona 2022).

The global atmospheric energy budget depends largely on exchanges of heat and moisture at the surface, which is controlled by turbulent fluxes in the PBL. Thus, the evolution and thermodynamic properties of the PBL have significant implications for the development of weather phenomena, such as storms, fog, and low-level clouds (Wilson et al. 1992; Ackerman et al. 1995; Medeiros et al. 2005). The foregoing discussion underscores the importance of understanding the key processes governing PBL development and incorporating them into numerical models to improve predictions of air quality, weather, and climate.

Bottom-up turbulent mixing driven by surface energy fluxes (e.g., sensible heat flux) is the primary driver of the PBL development. Surface energy fluxes vary not only with solar energy (e.g., season, latitude, clouds, and aerosols) but also with land-use type, vegetation coverage, and soil moisture (Li and Avissar 1994; Garratt 1994; Zeng et al. 2017). Sensible heat flux, the major surface energy flux contributing to the PBL development over land, responds directly to solar heating and influences the diurnal and seasonal evolution of the PBL (Garratt 1994; Stull 2012). Diurnally, PBL height (PBLH) peaks in the afternoon and becomes much shallower at night after shortwave radiation ceases. Seasonally, PBLH typically peaks in summer due to the highest surface solar

radiation flux. Another key process of turbulent mixing is the entrainment at the top of the PBL, which mixes air from the free troposphere into the boundary layer (Sullivan et al. 1998).

PBL development is also strongly influenced by the stability of the lower atmosphere and by circulations ranging from local to large scales that drive subsidence. For example, PBL development is impeded when the lower troposphere exhibits high static stability or a strong temperature inversion (Mahrt and Vickers 2006; Mahrt 2014), which can be driven by processes such as night-time radiative cooling and low-level cold-air advection. Synoptic-scale subsidence can enhance inversion at the top of the PBL and suppress PBL growth (Blay-Carreras et al. 2014; Caputi et al. 2023). It is well-known that the mountain-valley circulation can suppress the PBL development due to the subsidence caused by the radiation-induced valley wind; the effect reaches its maximum when the solar radiation effect is the strongest, resulting in a lower PBLH in the summer than expected, such as in California's central valley (CV) (Bianco et al. 2011; Faloona et al. 2020; Caputi et al. 2023). Meanwhile, along the western coasts of continents, PBLH is lower in spring and summer during onshore flow due to colder sea surface temperatures and higher during offshore flow (Anthes 1978; Pal and Lee 2019; Han et al. 2023). All of these studies indicate that multi-scale atmospheric processes and circulations can modify PBLH development, not only by impeding growth (e.g., large-scale subsidence) but also by altering the peak season, and that these effects can be region-dependent.

California's CV is surrounded by mountains, with the Coast Ranges to the west and the Sierra Nevada to the east. In addition to the mountain-valley wind mentioned above, other local processes can modulate PBL development in the CV, including the agricultural irrigation effect (Li et al. 2016; Yu et al. 2025) and the penetration of marine cold air by the Delta sea breeze (Bianco et al. 2011). Although the PBL development in the CV is complex and may be modulated by several factors, a lack of regular radiosonde observations in the CV limits our understanding of PBL characteristics in this area.

California's CV is an agriculturally productive region with a Mediterranean climate that receives little to no precipitation from late spring to early fall. Thus, irrigation is required to grow crops during this period. Agricultural irrigation can modify the partition of energy at the surface. Numerical studies have shown that irrigation increases soil

moisture but also modifies near-surface air humidity (increase) and temperature (decrease) via evapotranspiration (Sorooshian et al. 2011, 2012, 2014; Yang et al. 2017; Jackson 2021). As a result, the reduction in daytime surface sensible heat flux (Zeng et al. 2017) lowers the PBLH (Li et al. 2016; Yu et al. 2025).

Along the Coast Ranges, the terrain gap near the Sacramento-San Joaquin Delta allows marine air to penetrate the CV, known as the Delta sea breeze (Zhong et al. 2004; Mayor 2011; Bianco et al. 2011; Shapkalijevski M et al. 2017; Caputi et al. 2019). In summer, cold marine air is transported into the CV by the enhanced Delta sea breeze due to strong land-sea thermal contrast between the coast and the heated CV, leading to a strong inversion (i.e., high static stability) near the surface in the CV; in consequence, it not only lowers the night-time PBLH but also creates a stable layer, delaying the erosion by solar heating in the morning (Bianco et al. 2011). These marine air penetration events occur mostly in summer, when the temperature difference between outside (i.e., the coastal region) and inside the CV reaches an annual maximum (Wang and Ullrich 2018). Studies have shown that the shallower summertime PBLH observed at certain sites is consistent with enhanced stability, which may be linked to marine air penetration (MAP) influences (Bianco et al. 2011). However, these studies used either observational data or reanalysis data to qualitatively investigate marine air intrusion into the CV and discuss its impacts on PBL development. To the best of our knowledge, no prior study has used a numerical approach to quantify the MAP effect on PBLH development, which is a focus of the current study. In addition, although both agricultural irrigation and MAP can alter PBL development in the CV, their relative contributions to changes in PBLH have not been simultaneously compared, which is another focus of this study.

2 Numerical Experiments and Observations

2.1 Experimental design

One-week numerical simulations are designed to quantify the impacts of MAP and agricultural irrigation on near-surface meteorology and PBLH in California's CV. Figure 1a shows the time series of the daily maximum-mean PBLH, averaged from 1500–1700 LT (local time = UTC – 8 h, defined as Pacific Standard Time rather than Pacific Daylight Time in this study), for four stations in the CV for the month of July 2022. From early to

mid-July, PBLHs at Yuba City, Fresno, and Bakersfield are generally higher and more variable, indicating that clouds and synoptic- and mesoscale weather systems, in addition to diurnal forcing, influence PBLH. In contrast, during mid- to late-July, PBLHs are lower and less variable (Fig. 1a), suggesting that fewer transient weather systems pass over the region and that diurnal forcing dominates PBL development. Since the study compares the impact of cold MAP versus agricultural irrigation on PBLHs in the CV, both of which are driven primarily by diurnal forcing, a late-July period from 21 to 27 July 2022 (UTC), is selected to minimize interference from clouds and transient weather systems.

The year 2022 was chosen because ceilometers operated by the California Air Resources Board (CARB) in the CV provide the most comprehensive dataset for model evaluation.

Four numerical simulations (Table 1) are conducted using the Weather Research and Forecasting (WRF)-irrigation model (Yu et al. 2025). The four experiments differ in the combinations of two settings: 1) filling mountains (FM) at gaps along the coastal range at the western side of the CV versus using the original terrain, and 2) integrating the model with the agricultural irrigation (WIR) versus without (WoIR). In the FM experiments, the coastal mountain ridge is raised to a minimum elevation of 700 m (Figs. 2a–c) to minimize cold MAP into the CV. Note that the 700 m is chosen after trial and error to prevent cold marine air from flowing over the mountain into the CV and minimize mountain wave activity. Along the coastal range, the Sacramento-San Joaquin Delta provides the primary pathway for the strongest MAP, while the gap (with the lowest elevation of 350 m) at the Pacheco Pass (near 37°N, 121°W) contributes a secondary, much weaker cold-air inflow than the primary one (Fig. 1b, c). In contrast, the smaller gap near 32.5°N, 120.5°W (with the lowest elevation of 580 m) contributes minimally to MAP.

In WIR, irrigation is applied once every three days, with each model point receiving a randomly assigned first irrigation day. A county-level irrigation rate of 1.3–3.0 mm day-1 is used. Irrigation starts at 0600 LT and lasts for 4 hours on the irrigation dates. The model includes three irrigation methods–sprinkler, drip, and flood–that use different percentages of the irrigated water and place water at different model levels. The irrigation information is based on the U.S. Geological Survey (USGS) water-use report. Details of the irrigation parameterization are referred to Yu et al. (2025).

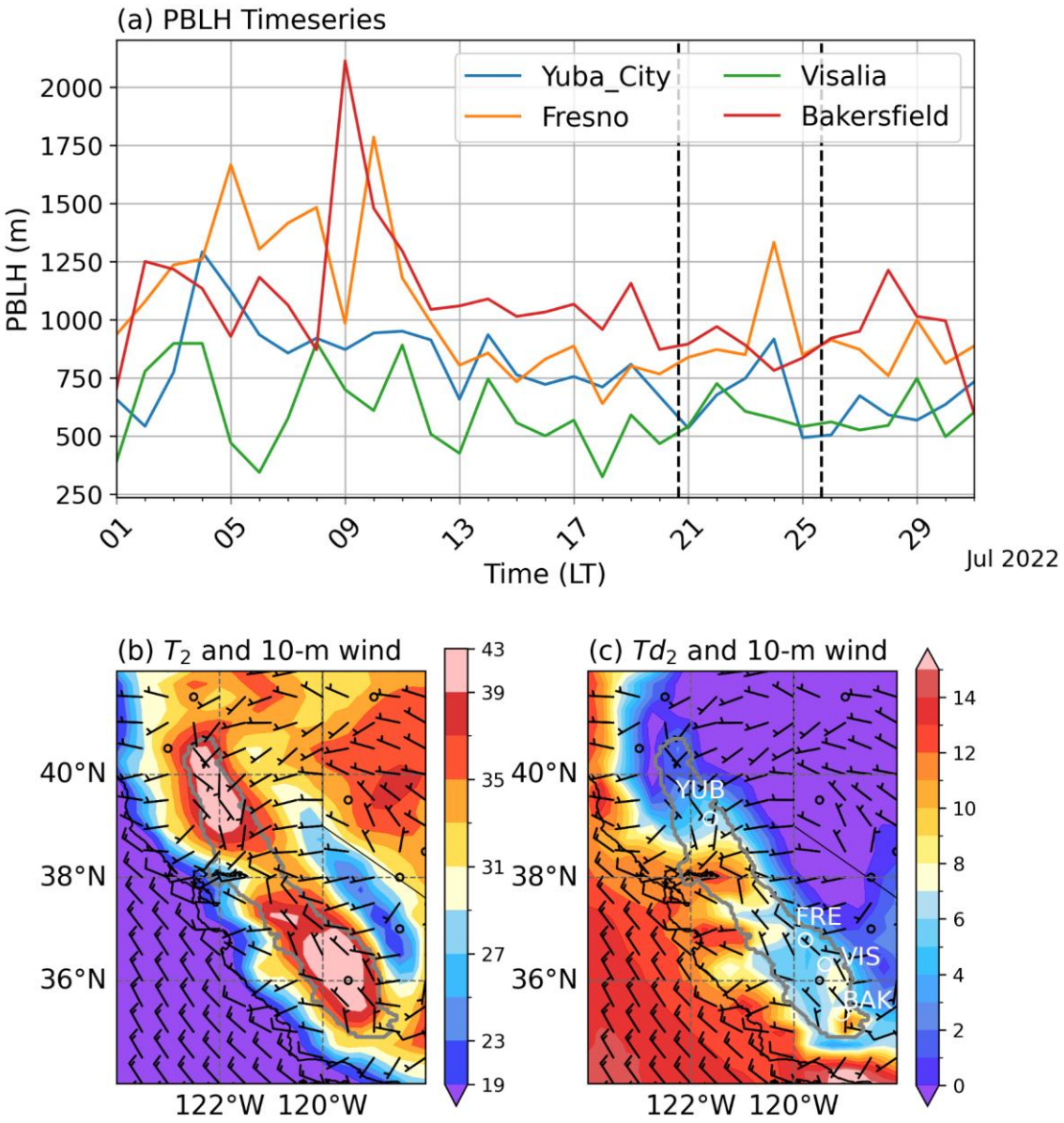


Fig. 1 (a) Time series of ceilometer-derived daily-maximum PBLHs at different sites in July 2022. The daily maximum PBLHs are averaged from 1500 to 1700 LT, when the PBLHs are the highest. The ceilometer sites are labeled in Fig. 1c, and they are, from north to south, Yuba City (YUB), Fresno (FRE), Visalia (VIS), and Bakersfield (BAK). The three-hourly (1500–1700 LT) average of (b) 2-m temperature (T_2), and (c) 2-m dew point temperature (Td_2) overlapped with 10-m wind from ERA5 3-h forecast data during the simulation period, 21–27 July 2022 00UTC (between two dashed lines in (a)).

For each experiment, there are two nested domains (D01 and D02) with horizontal resolutions of 12 and 4 km, and 208×190 and 343×319 grids, respectively, in the x–y directions. Vertically, the model uses 45 stretched terrain-following levels with a higher resolution near the surface. The model top is at 100 hPa, and a two-way interaction between domains is applied. The WRF parameterizations are listed in Table 2.

The initial and lateral boundary conditions for WRF simulations are provided by the European Centre for Medium-Range Weather Forecasts (ECMWF) version 5 Reanalysis (ERA5) dataset, which has a horizontal resolution of 0.25° and a temporal resolution of 1 hour.

Because the ERA5 dataset does not account for irrigation, two one-month simulations from 20 June to 21 July, before the model's initial time, are conducted to spin up soil moisture and temperature. The spin-up runs use the same configuration as their corresponding WIR and WoIR, except that four-dimensional data assimilation (FDDA) is applied to both domains to nudge the model's wind, temperature, and moisture above the PBL toward ERA5 reanalysis (Seaman et al. 1995). The final states from the one-month run are used to initialize the soil moisture and soil temperature fields of their corresponding WIR and WoIR runs (Table 1). Note that FDDA is not applied to the four numerical experiments in Table 1.

Table 1 Experimental settings for numerical experiments in the study. The Filled-Mountain (FM) experiment is to raise the elevation of the mountain ridge/gaps to a minimum of 700 m along the coastal range on the western side of the CV.

WRF Experiments	Irrigation (IR)	Filled-Mountain (FM)
WoIR	off	off
WIR	on	off
WoIR_FM	off	on
WIR_FM	on	on

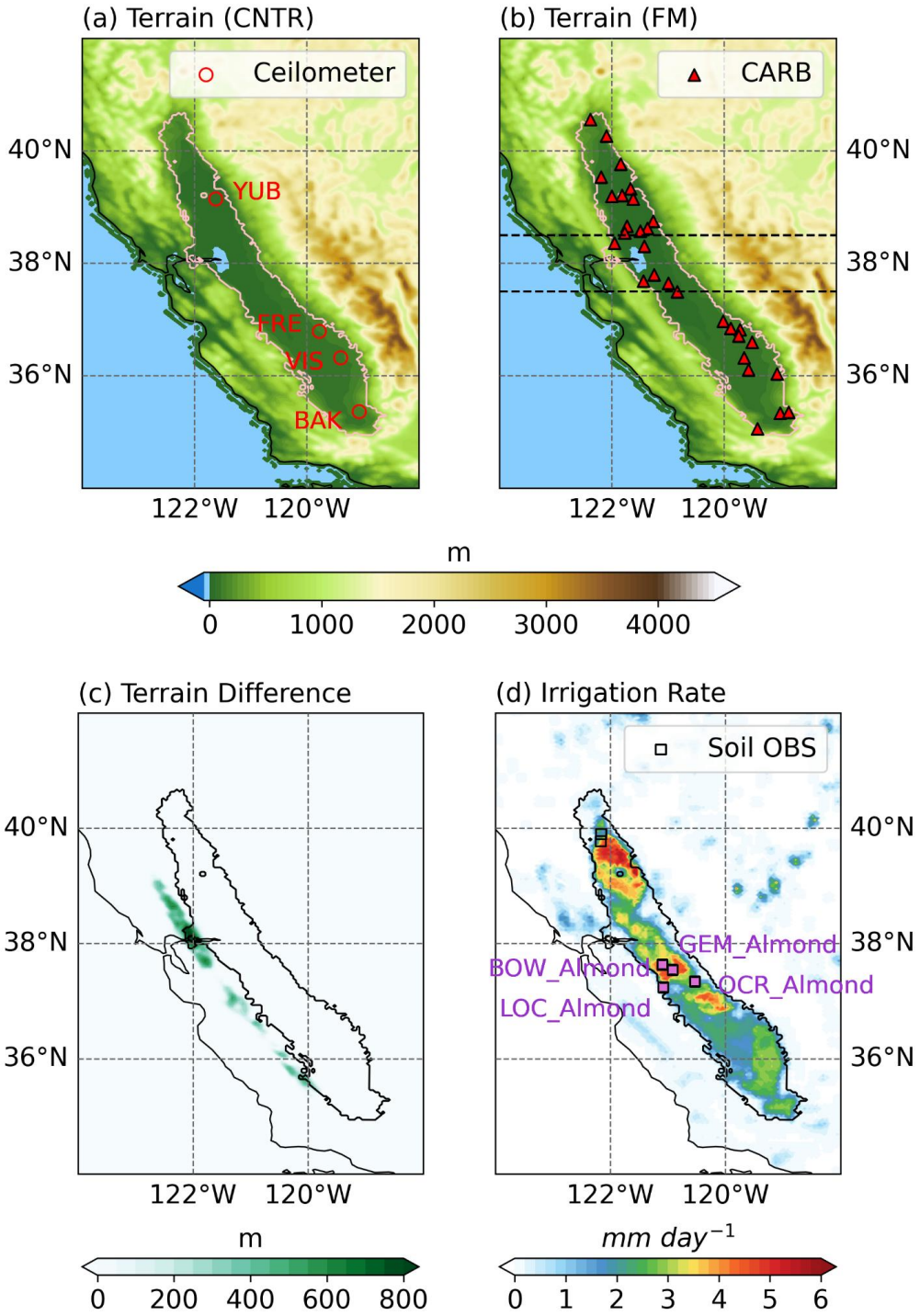


Fig. 2 (a) The original terrain, (b) filled-mountain (FM) terrain, and (c) the difference between (b) and (a). (d) The irrigation rate used in model simulations. Ceilometer sites (circles) for PBLH are labeled in (a). The surface observational sites from CARB (triangles) are labeled in (b). The *in situ* soil observational sites (squares) are labeled in (d). The purple squares in (d) denote BOW_Almond, GEM_Almond, LOC_Almond, and OCR_Almond stations.

Table 2 Physics parameterizations used in WRF simulations.

WRF parameterization		References
Surface Scheme	Revised MM5 Monin-Obukhov	(Jiménez et al. 2012)
PBL Scheme	YSU	(Hong et al. 2006)
Microphysics Scheme	WSM6	(Hong and Lim 2006)
Radiation Scheme	RRTMG	(Iacono et al. 2008)
Cumulus Scheme	new Tiedtke (D01 only)	(Zhang and Wang 2017)

2.2 Observations

Observations are used to evaluate model results, including soil moisture, soil temperature, and PBLH. Soil moisture and temperature measurements were taken from *in situ* instruments at six sites in the CV (see Fig. 2d for the locations). Soil moisture is measured as point volumetric water content using the EC-5 sensor. In addition, the Averaging Soil Thermocouple Probe, TCAV-L, provides an average temperature of the top 5 cm of the soil layer. Hourly daytime PBLH observations (CARB-PBLH) are derived from aerosol backscatter profiles measured by CARB's ceilometer network. A Haar wavelet transform method was utilized to detect vertically localized maxima of the aerosol backscatter gradient (Caicedo et al. 2020). A temporal continuity metric is also applied to retain physical accuracy of the PBLH diurnal cycle.

3 Results and Discussion

We first examined the effects of irrigation (i.e., WIR versus WoIR) and MAP (i.e., WIR versus WIR_FM) individually on the changes in near-surface meteorology and PBLHs in the CV. We then compared the relative contributions of the two effects to PBLH changes and examined how and why these contributions vary across the CV. Observations from 22 to 26 July, corresponding to 36-h to 156-h forecasts, are used to evaluate the model's performance. To discuss the spatial variation across the CV, we define northern CV as the northern tip to 38.5°N, central CV as 38.5°–37.5°N, and southern CV as 37.5°N to the southern tip of the CV.

3.1 Irrigation Effects

The one-week simulation results from WIR, the most realistic among the four experiments, are evaluated against the observations presented in Section 2.2 to assess model fidelity, and compared with those from WoIR to assess the irrigation effect on near-

surface meteorology and PBLH. The evaluation strategies (e.g., bias and root-mean-square error (RMSE)) for model forecasts are similar to those in Yu et al. (2025), except that ours are one-week simulations, whereas theirs are three-month simulations. Note that the bias is averaged over 0300–0500 and 1500–1700 LT when the differences between WIR and WoIR are maximal, and the RMSE is computed over all hours.

3.1.1 Soil moisture and temperature

Compared with WoIR, WIR has higher soil moisture (*SMOIS*) and overall cooler soil temperature (T_{soil}) in the first soil layer (0–10 cm depth). The maximum difference in 1st-layer *SMOIS* is about 0.20 $m^3\ m^{-3}$ in the northern CV and 0.10 $m^3\ m^{-3}$ in the southern CV (figure not shown). Evaluated against *in situ* observations (see station locations in Fig. 2d), the inclusion of the irrigation effect corrects night-time (0300–0500 LT) bias of the first-layer *SMOIS* (T_{soil}) from -0.10 $m^3\ m^{-3}$ (2.81 K) in WoIR to 0.03 $m^3\ m^{-3}$ (0.40 K) in WIR, the daytime (1500–1700 LT) bias from -0.10 $m^3\ m^{-3}$ (6.32 K) in WoIR to 0.04 $m^3\ m^{-3}$ (6.23 K) in WIR, and RMSE of the first-layer *SMOIS* (T_{soil}) from 0.12 $m^3\ m^{-3}$ (5.49 K) in WoIR to 0.06 $m^3\ m^{-3}$ (4.51K) in WIR.

3.1.2 2-m temperature (T_2) and 2-m dew point temperature (Td_2)

Figure 3 shows the average of T_2 and Td_2 differences between WIR and WoIR at 1500–1700 LT and 0300–0500 LT. Irrigation cools T_2 during the day due to increased evapotranspiration, and warms it at night in the CV (Fig. 3a, b). The night-time warmer T_2 in WIR is due to the upward ground surface energy flux (Yu et al., 2025). The largest T_2 differences are located in the northern and southern CV, consistent with the higher irrigation rate (Fig. 2d). A minimum T_2 difference between the two experiments occurs along the 38.5 °N zone, where low-level temperature change is dominated by marine cold-air advection rather than irrigation.

Irrigation increases Td_2 during the daytime because of higher evapotranspiration in WIR than in WoIR (Fig. 3c). At night (0300–0500 LT), the difference in Td_2 decreases because evapotranspiration is nearly sealed. However, the moistened air in WIR is advected by the strong north-northwesterly winds, accumulating more moisture at the end of the southern CV (Fig. 3d).

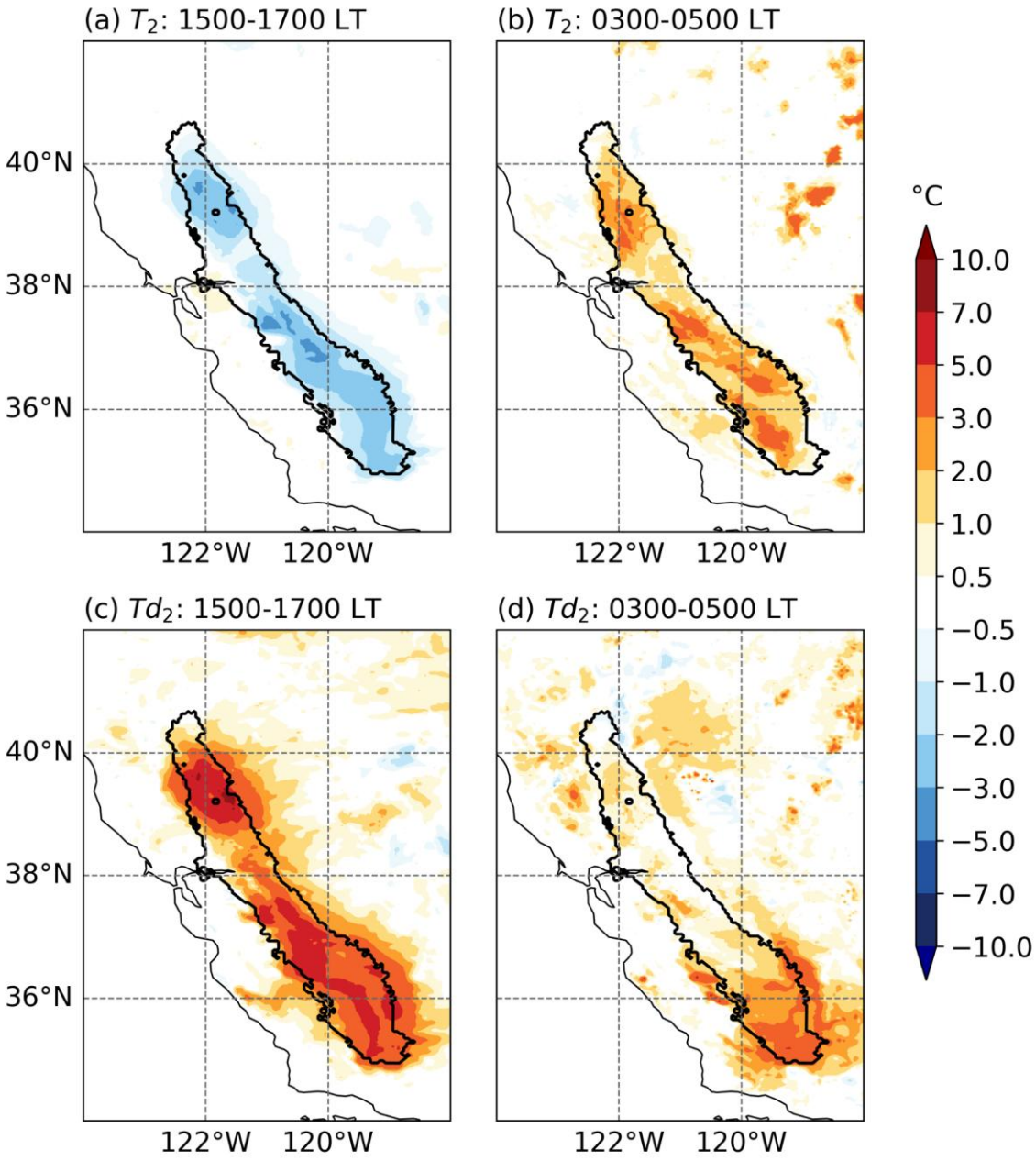


Fig. 3 Average of (a, b) T_2 and (c, d) Td_2 differences between WIR and WoIR at 1500–1700 LT (left) and 0300–0500 LT (right) from 22 to 26 July 2022.

Compared to CARB observations (see station locations in Fig. 2b), the warmer T_2 forecast bias at 1500–1700 LT in WoIR is reduced by 1 °C after the inclusion of the irrigation effect. At night, T_2 forecast bias in the CV is improved by 0.56 °C; however, the irrigation-induced warming effect overcorrects the cold bias in WoIR to a slightly warm bias in WIR in both northern and southern CV. The RMSE reduction for T_2 is statistically significant (p-value = 0.0005) using the paired-sample T-test across all sites. With respect

to Td_2, compared with WoIR, daytime Td_2 bias at 1500–1700 LT is substantially reduced by irrigation by 2.25 ºC. However, at night, the Td_2 bias worsens slightly in WIR. The positive bias in both WoIR and WIR is mainly attributable to the northern CV sites, because the night-time southerly wind contributed by the Delta sea breeze in the northern CV is 1–2 ms^{-1} stronger in the simulations than observations (figure not shown). Despite the slight increase in night-time Td_2 bias at 0300–0500 LT, the RMSE of Td_2 is reduced significantly (p-value = 0.0001) since the daytime Td_2 bias reduction dominates.

Table 3 Root-mean-square-error (RMSE) and bias diagnostics for T_2 and Td_2 in WIR and WoIR in the CV. The differences of RMSE in WIR and WoIR are calculated. Increased biases in WIR are denoted as bold numbers. Note that the bias is averaged over 0300–0500 and 1500–1700 LT, and the RMSE is computed over all hours.

T_2	RMSE			Bias			
# of sites	WIR	WoIR	WIR - WoIR	WIR 0300–0500 LT	WoIR 0300–0500 LT	WIR 1500–1700 LT	WoIR 1500–1700 LT
31	2.84	3.35	-0.52	0.53	-1.09	1.01	2.01
Td_2	RMSE			Bias			
# of sites	WIR	WoIR	WIR - WoIR	WIR 0300–0005 LT	WoIR 0300–0500 LT	WIR 1500–1700 LT	WoIR 1500–1700 LT
18	3.85	4.81	-0.96	**0.60**	0.04	-2.04	-4.29

Overall, the irrigation effects on near-surface meteorology obtained in this study are reasonable and similar to those reported by Yu et al. (2025). The overall results indicate that it is reasonable to use WIR as our baseline experiment to assess the effects of irrigation and MAP on changes in PBLH in the study.

3.1.3 PBLHs

Irrigation not only reduces the diurnal T_2 difference but also affects lower-atmosphere stability during both daytime and night-time, thereby influencing PBL development. The diurnal cycles of lower-atmospheric stability (e.g., vertical virtual potential temperature gradient) and PBLH at Yuba City and Fresno are used to illustrate the changes by irrigation (Fig. 4).

The lower atmosphere is stable (i.e., inversion) at night due to longwave radiative cooling. Compared to WoIR, irrigation destabilizes the lower atmosphere at night (blue shading in Fig. 4c, d) due to warmer near surface temperature caused by upward ground heat flux, as discussed earlier. During the daytime, PBLH in WIR is lower due to reduced sensible heat flux by irrigation and is closer to the observations than in WoIR. In contrast to these pronounced day-night differences, the early phase of PBL development between WoIR and WIR does not differ significantly until 1000–1100 LT because the effects of night-time destabilization and the reduced sensible heat flux in the morning in WIR offset one another.

Consistent with previous observational studies, our diurnal lapse rate of virtual potential temperature in Chico in WIR (figure not shown) is similar to that in Bianco et al. (2011), which presented a monthly-average result (15–21 K km^{-1} at 400–500 m a.g.l.) derived from Radio Acoustic Sounding Systems (RASS).

We further examine the spatial distribution of the PBLH change due to irrigation. In WoIR, the average PBLH is generally higher in the northern CV, and between 36°N and 37°N (Fig. 5a). Compared to WoIR, the PBLH is reduced across the CV in WIR, except for the central CV, where the MAP effect dominates (Fig. 5). The spatial pattern of the PBLH reduction matches the T_2 daytime difference between the two experiments (Fig. 3a). Irrigation lowers the PBLH by more than 0.5 km in the northern CV, with the strongest reduction by ~1.5 km near Willows (39.53°N, 122.19°W), and by 0.5 to 1 km in the southern CV (Fig. 5c).

In terms of model performance, PBLH forecast in WIR is improved compared to WoIR. The averaged PBLH RMSE at Yuba City and Fresno drops from 508 m in WoIR to 201 m in WIR, despite a positive bias relative to the CARB-PBLH in both experiments (Fig. 4). In Fig. 5, the individual RMSE at each site shows the largest improvement at Yuba City

(RMSE of 877.6 m for WoIR and 319.8 m for WIR), and the lowest RMSE at Fresno in WIR. Generally, irrigation effects are stronger in Yuba City than in Fresno, consistent with the spatial distribution of irrigation rates (Fig. 2d) and the soil moisture difference between WIR and WoIR (figure not shown).

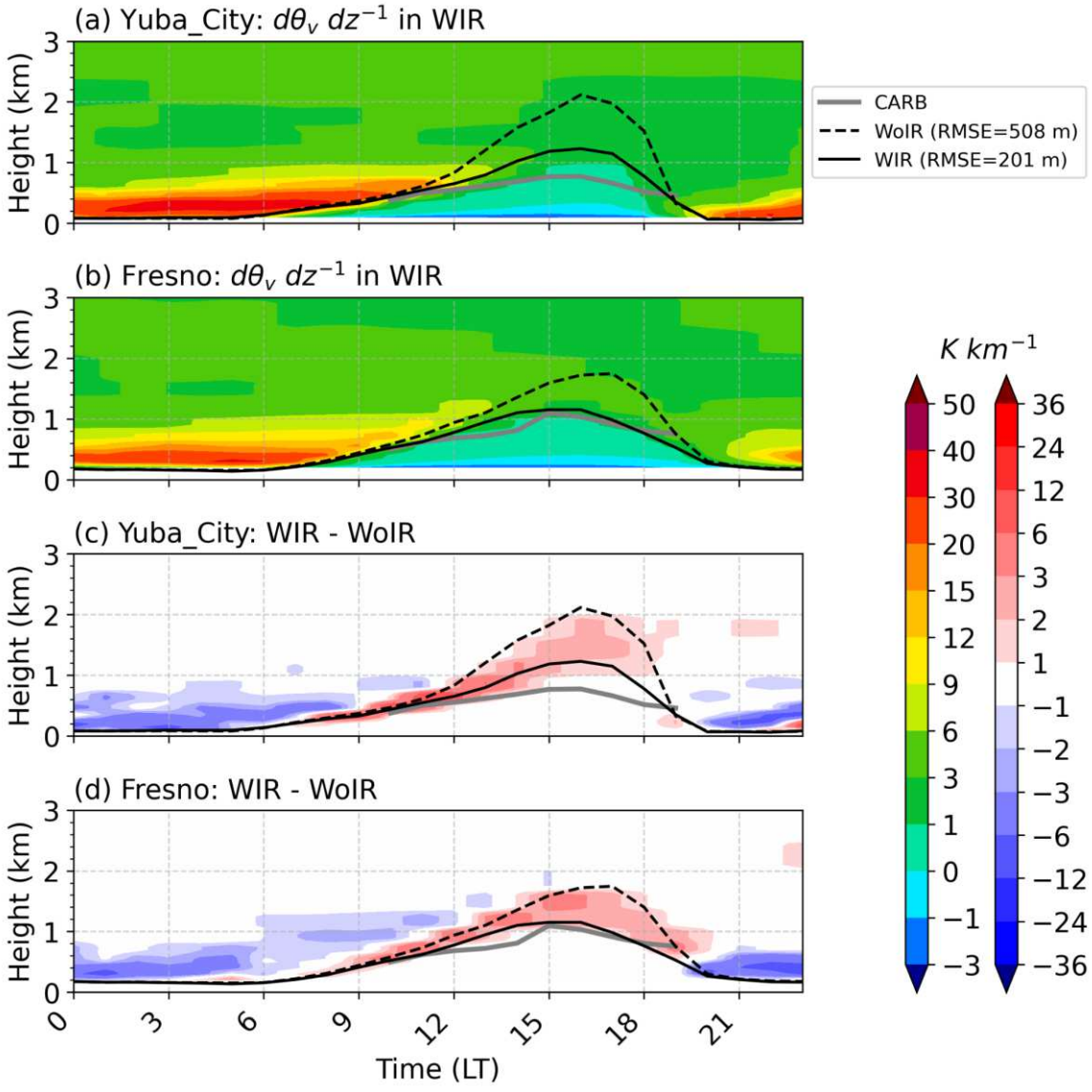


Fig. 4 Diurnal cycle of virtual potential temperature (θ_v) gradients (shaded; K km^{-1}), averaged over 22–26 July 2022 LT, for (a, b) WIR and (c,d) the difference between WIR and WoIR (WIR - WoIR). (a, c) are for Yuba City and (b, d) for Fresno. The lines show the PBLH diurnal cycles from WIR, WoIR, and the observation (CARB-PBLH) at the corresponding station in each figure. The averaged RMSEs of PBLH at Yuba City and Fresno in WoIR and WIR are labeled.

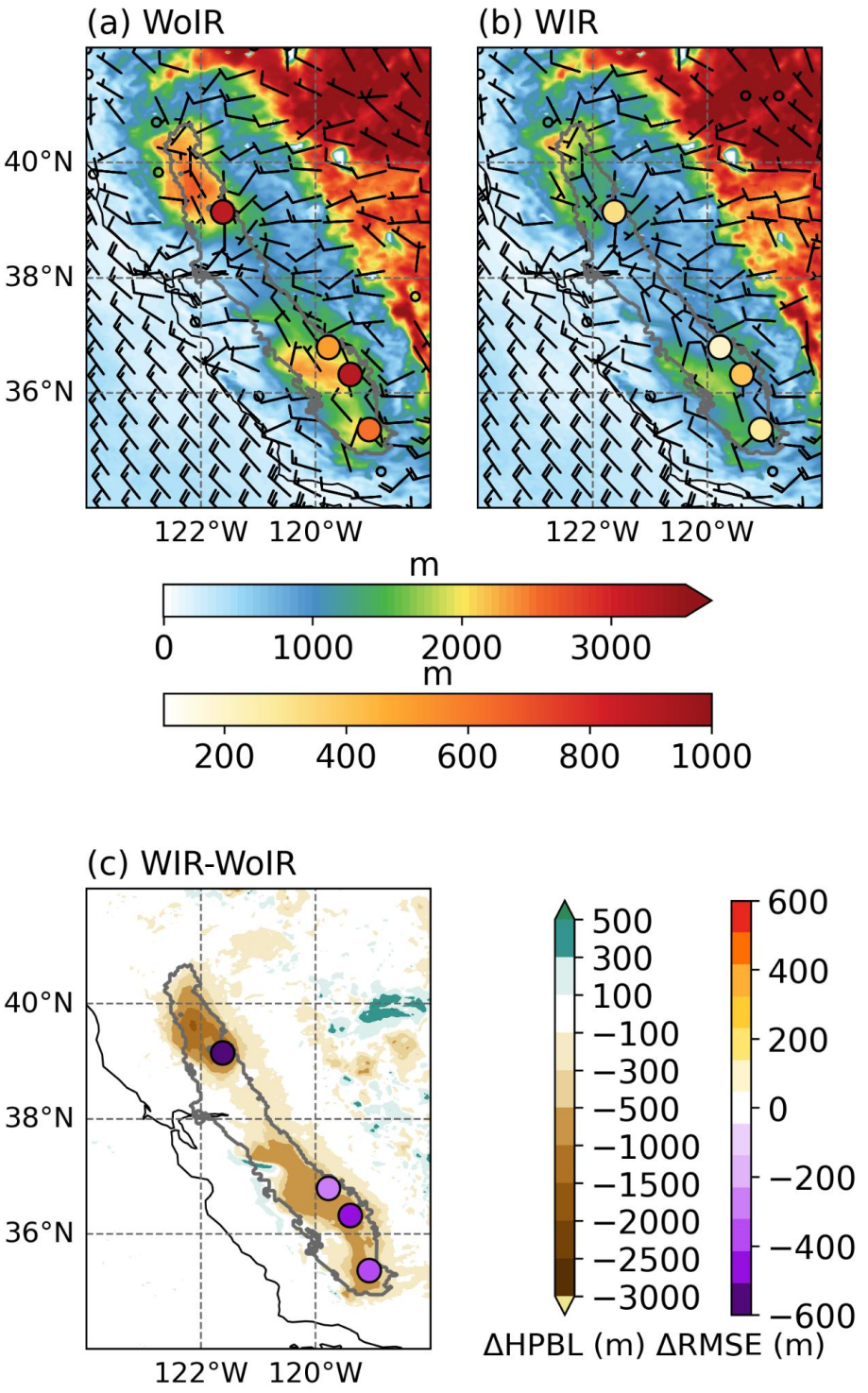


Fig. 5 Three-hourly average PBLH and 4th model-level wind for (a) WoIR and (b) WIR, and (c) the PBLH difference between WIR and WoIR, at 1500–1700 LT from 22 to 26 July 2022. Filled circles show the root-mean-square-error (RMSE) of PBLH relative to CARB-PBLH in (a) WoIR, (b) WIR, and (c) the RMSE differences between WIR and WoIR.

306 **3.2 MAP Effects**

307 Unlike the irrigation analysis using 5-day results, we evaluate the MAP effect based on
308 FM results from 23–24 July 2022 LT. This is because model results indicate that, on other
309 days, terrain modification can drive mountain-wave activity in the lower atmosphere in the
310 CV, which can influence PBLH and make it difficult to isolate the MAP effect. Thus, all
311 figures shown in this section are the average of these two days (i.e., 23–24 July), unless
312 specified.

313 *3.2.1 T_2 and Td_2*

314 The MAP effect advects cold and moist air from the coast into the CV and is quantified
315 by comparing the differences between WIR and WIR_FM. The MAP effect makes T_2
316 colder across the CV at both day (1500–1700 LT) and night (0300–0500 LT), with the
317 maximum impact near the central CV, where the MAP primary source is, and decreasing
318 toward both northern and southern ends of the CV (Fig. 6a, b). The daytime cooling effect
319 mainly extends southward from the Delta MAP entrance, with another local maximum near
320 Pacheco Pass (i.e., the secondary MAP; Fig. 6a, c), implying that the MAP air is mostly
321 advected southward during the daytime. In contrast, the night-time cooling effect by MAP
322 forms a sector-shaped feature centred at the Delta gap (i.e., the MAP source), extending
323 both northward and southward with air temperature change slightly colder on the northern
324 side (Fig. 6b). This implies that the MAP air is advected both southward and northward at
325 night after entering the CV.

326 Similarly, the low-level moisture, e.g., Td_2, in the CV is higher in WIR than in
327 WIR_FM, with a local maximum near the MAP entrances and decreasing toward the
328 northern and southern ends of the CV (Fig. 6c, d). This again indicates that the MAP effect
329 can influence the entire CV (Fig. 6), and the effect decreases with increasing distance from
330 the MAP entrance.

331 During the daytime at 1500–1700 LT, colder temperatures and higher humidity
332 associated with MAP in WIR extend to the upslope of the Sierra Nevada due to advection
333 by thermally driven valley winds (Fig. 6a, c). At night (0300–0500 LT), the cooling and
334 moistening effect near the surface is stronger than during the day (Fig. 6a,c versus 6b,d)
335 because a deeper PBL during the daytime dilutes the MAP effects.

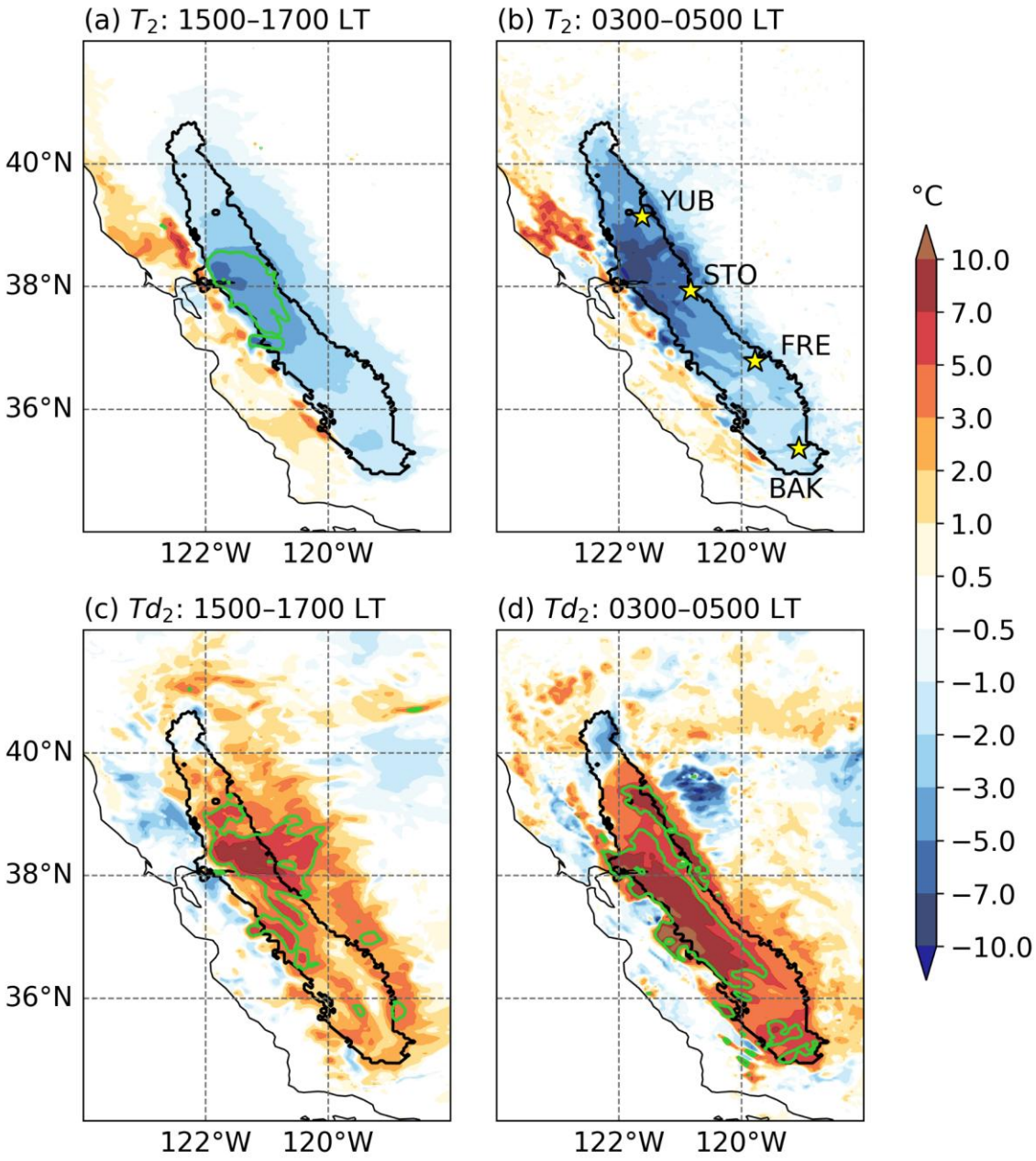


Fig. 6 Average of (a, b) T_2 and (c, d) Td_2 differences between WIR and WIR_FM at 1500– 1700 LT (left) and 0300– 0500 LT (right) from 23 to 24 July 2022. The green contours in (a), (c), and (d) are T_2=-3.5 °C, Td_2=4.3 °C and Td_2=5.9 °C, respectively. The four yellow stars in (b) indicate locations of Yuba City (YUB), Stockton (STO), Fresno (FRE), and Bakersfield (BAK), where model fields were extracted for plots in Fig. 9.

Because advection depends on wind and the gradient of the transported field, we also examine the wind field together with temperature and moisture. During the daytime, the northern CV is calm in both WIR and WIR_FM, with valley-wind dominance around the

upslopes (Fig. 7). In WIR, MAP increases westerly wind over open gap regions, which turns toward south, producing more consistent north-northwesterly flow in the central CV than in WIR_FM (Fig. 7). In consequence, the northern part of the southern CV (36.5°N–37.5°N, hereafter Nor-SCV) is still dominated by north-northwesterly flow that becomes weaker toward south of 36.5°N, where air mass accumulates (Fig. 7). As a result, the daytime MAP-wind in WIR mainly advects cold, moist marine air eastward and southward in the CV. On the other hand, without MAP air flowing into the CV, the wind in the southern CV is calmer and the temperature gradient is weaker in WIR_FM than in WIR (Fig. 7a, b). Thus, the daytime cooling effect due to MAP between WIR and WIR_FM is more pronounced in the central and Nor-SCV than in the northern CV, attributable to both wind and temperature gradient fields (Fig. 6a).

While the MAP impact on moisture presents similar results to that on temperature, unlike temperature, which is affected not only by MAP but also by radiative and adiabatic processes, moisture, as a tracer, shows a different spatial pattern than that of temperature. Figure 6c shows that the daytime moistening effect extends from the central CV not only into the southern CV but also further eastward into the mountains, where the latter is related to the stronger westerly flow and higher moisture in the central CV during the day in WIR than in WIR_FM (Fig. 7c versus 7d).

At night, wind patterns in WIR and WIR_FM are quite different in the northern CV (Fig. 8a, c versus 8b, d). The southerly wind is present in the northern CV in WIR but is almost absent in WIR_FM. Thus, MAP-driven southerly wind advects cold air into the northern CV in WIR (Fig. 6b). It is noticed that the night-time moisture is slightly higher in WIR_FM than in WIR close to the northern end of the CV (Fig. 6d). This is attributed not only to the MAP effect being much weaker in the area but also to slight changes in diurnal mountain winds (Fig. 8c versus 8d).

In the central and southern CV, the north-northwesterly winds are strong at night in both WIR and WIR_FM, with WIR exhibiting slightly higher wind speeds, particularly in the central CV, due to the MAP effect (Fig. 8). In addition, the night-time north–south temperature (Fig. 8a, b) and moisture (Fig. 8c, d) gradients are larger in WIR than in WIR_FM. Stronger winds and larger temperature and moisture gradients in WIR than in

WIR_FM together lead to strong night-time cooling and moistening effects by MAP in the southern CV (Fig. 6b, d).

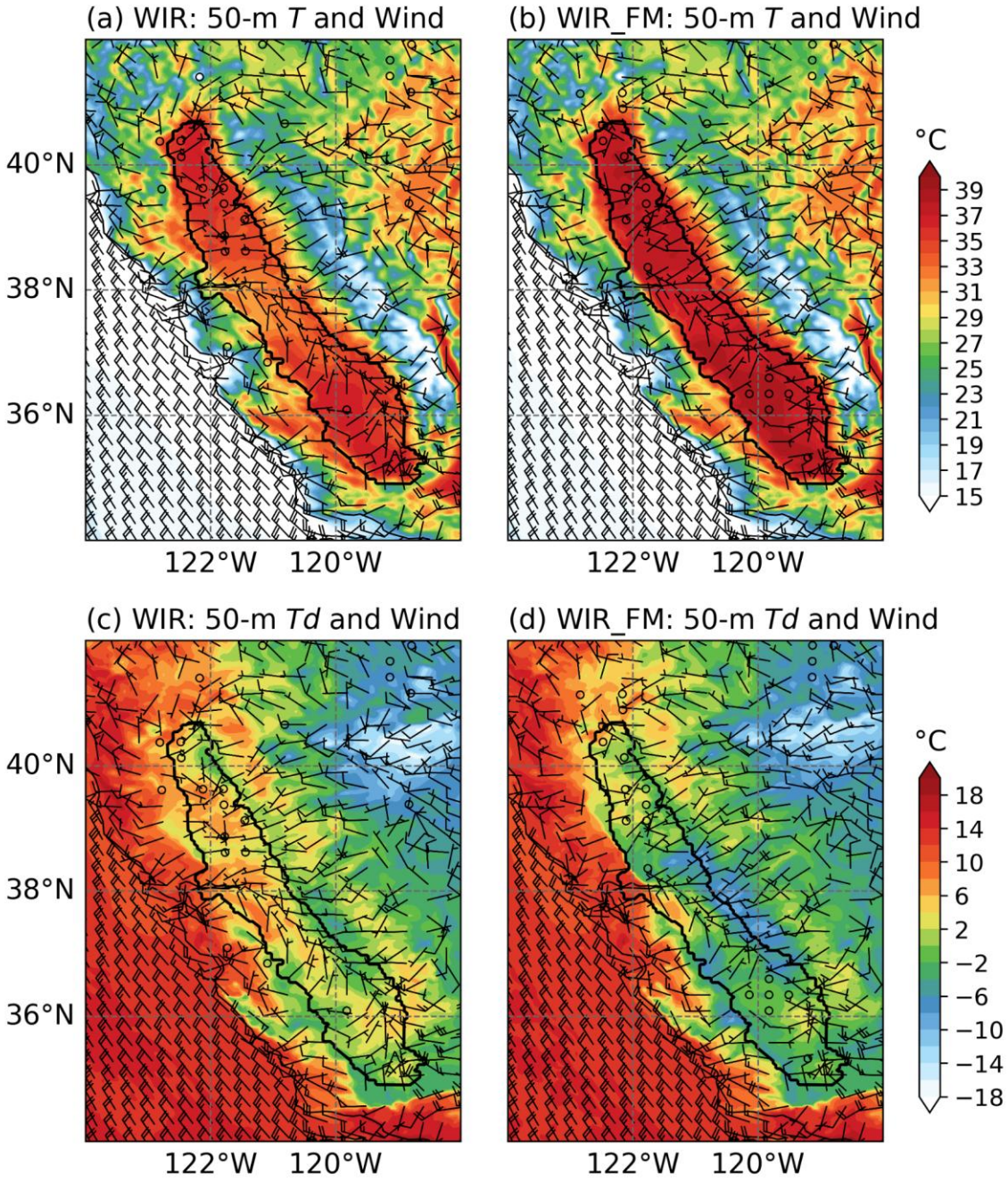


Fig. 7 Average of (a, b) 50-m temperature and (c, d) 50-m dew point temperature (unit: °C), overlapped with horizontal winds (units: knots), from (a, c) WIR and (b, d) WIR_FM at 1500 LT from 23 to 24 July 2022.

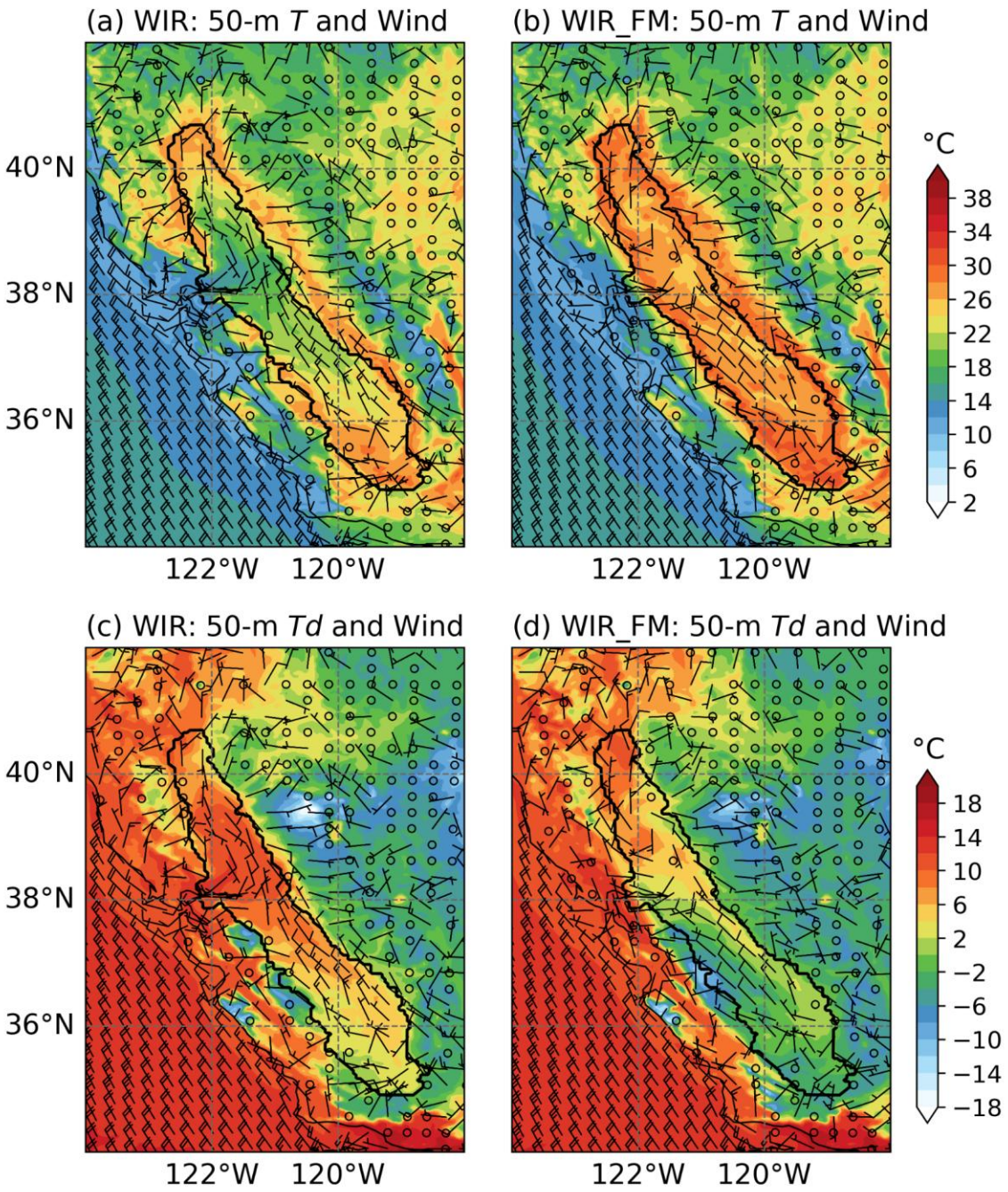


Fig. 8 Same as Fig. 7 but at 0300 LT.

3.2.2 PBLHs

To quantify the diurnal cycle of the MAP-induced stability change and the resultant PBL development change, the vertical virtual potential temperature gradient differences between WIR and WIR_FM in the lower atmosphere at four locations–Yuba City, Stockton, Fresno, and Bakersfield (see Fig. 6b for locations)–are presented (Fig. 9). The

strongest night-time inversion is located at about 300–400 m height a.g.l. at all four locations (Figs. 4a, b; 9a, b), with the weakest inversion in Backersfield. Stabilization by MAP suppresses PBL development across the CV (Figs. 9c–f). It is noticed that, compared to WIR_FM, a very thin, near-surface layer is destabilized by MAP at night, which is due to upward sensible heat flux (30–50 W m^{-2}) caused by the cold MAP air advected over the warm surface in the CV.

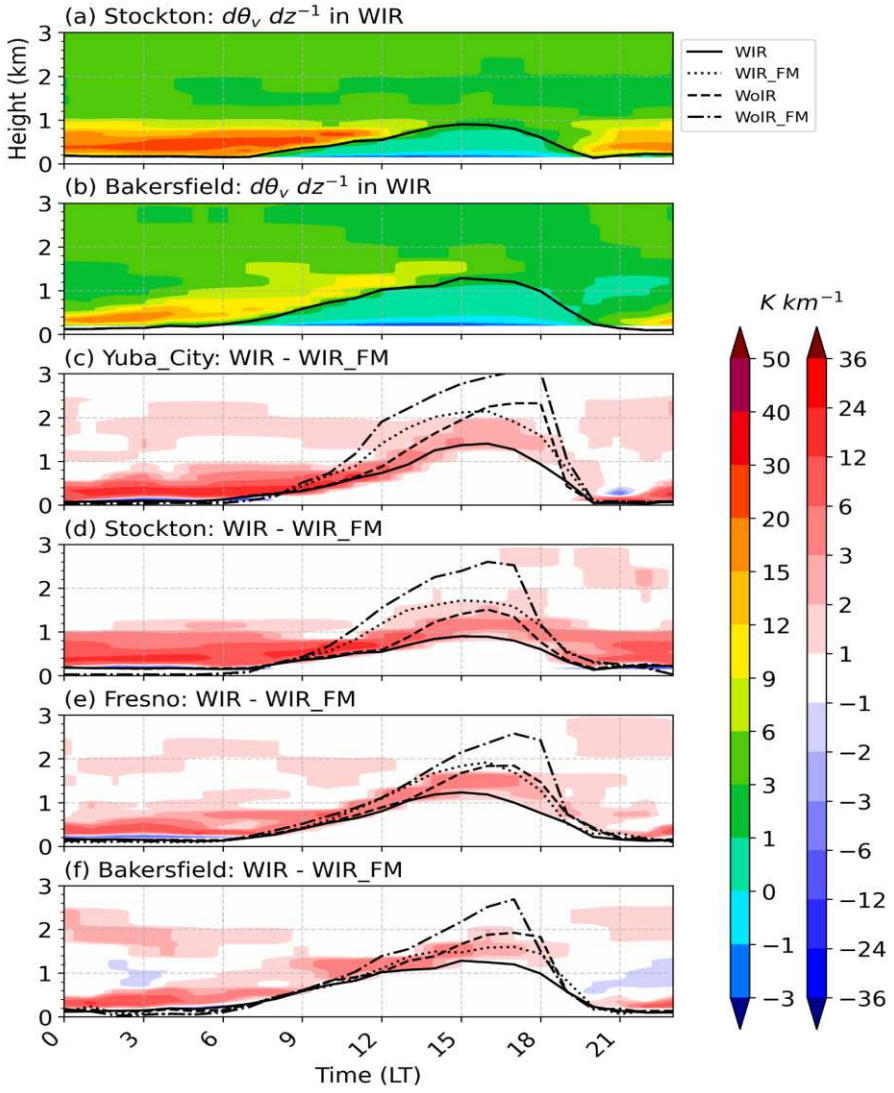


Fig. 9 Diurnal cycle of vertical virtual potential temperature (θ_v) gradients (units: K km^{-1}) from WIR at (a) Stockton, (b) Bakersfield, averaged over 23–24 July 2022 LT. The θ_v gradient differences between WIR and WIR_FM (units: K km^{-1}) at (c) Yuba City, (d) Stockton, (e) Fresno and (f) Bakersfield, averaged over 23–24 July 2022 LT, are plotted. Solid lines denote PBLH from WIR; dotted lines indicate PBLH from WIR_FM; dashed lines are PBLH from WIR; dashdot lines are PBLH from WoIR_FM. All sites are displayed as yellow stars in Fig. 6b.

MAP-induced stabilization and PBLH reduction vary by location. First, we note that while the southerly wind is very weak in northern CV during the daytime, night-time cold-air advection by MAP stabilizes the lower atmosphere and slows PBL development during the daytime (e.g., Yuba City). Yuba City and Stockton, both located at the edge of the cooling effect sector (Fig. 6b), are at a similar distance from the MAP source, so the MAP effect on night-time stability and daytime PBLH changes at both sites are similar (solid versus dotted lines in Fig. 9c, d). The stabilization effect by MAP weakens, and PBLH reduction lessens toward the south (Fig. 9e, f), explained by their relative distance from the Delta MAP source. This spatial pattern can also be verified in the MAP-induced PBLH changes shown in Fig. 10. In addition, compared to Stockton's, Yuba City's inversion layer at the PBL top in WIR and the stabilization layer in the lower atmosphere due to the MAP effect are much shallower (Figs. 4a; 9a, c, d), which will be discussed in Section 3.2.3.

The spatial pattern of the PBLH change by MAP is examined. The MAP effect decreases PBLH across most of the CV from the northern end of the CV to around 36.5°N by 0.5–1 km, with the largest PBLH reduction at 38.5°N (Fig. 10b) near the primary MAP entrance (Fig. 1b, c). The PBLH reduction tongue (36.5°N–37°N) extending from Pacheco Pass southeastward to Fresno is due to the secondary MAP source (Fig. 1b, c). The MAP-induced PBLH reduction is negligible (less than 0.5 m) in the southern part of the southern CV (35°N–36.5°N, hereafter Sou-SCV), significantly different from the rest of the CV (Fig. 10b).

The spatial pattern of PBLH reduction caused by MAP (Fig. 10b) matches well with the T_2 differences (Fig. 6a, b; green contours of T_2 = -3.5 °C in Fig. 6a), where the primary (secondary) MAP entrance contributes to stronger (weaker) and more widespread (limited) cooling effects near Delta (Pacheco Pass). The Td_2 difference can again verify the MAP effects through these two entrances (Fig. 6c, d; green contours of Td_2 = 4.3 °C in Fig. 6c and Td_2 = 5.9 °C in Fig. 6d). Trajectory analysis will be used later in Section 3.2.3 to show how the sea breeze brings marine air mass into the CV.

Similar to the daytime cooling and moistening effects by MAP, the PBLH reduction area caused by the MAP effect also extends to the western slopes of the Sierra Mountains (Fig. 10b), due to higher-PBLH advection by valley winds in WIR_FM.

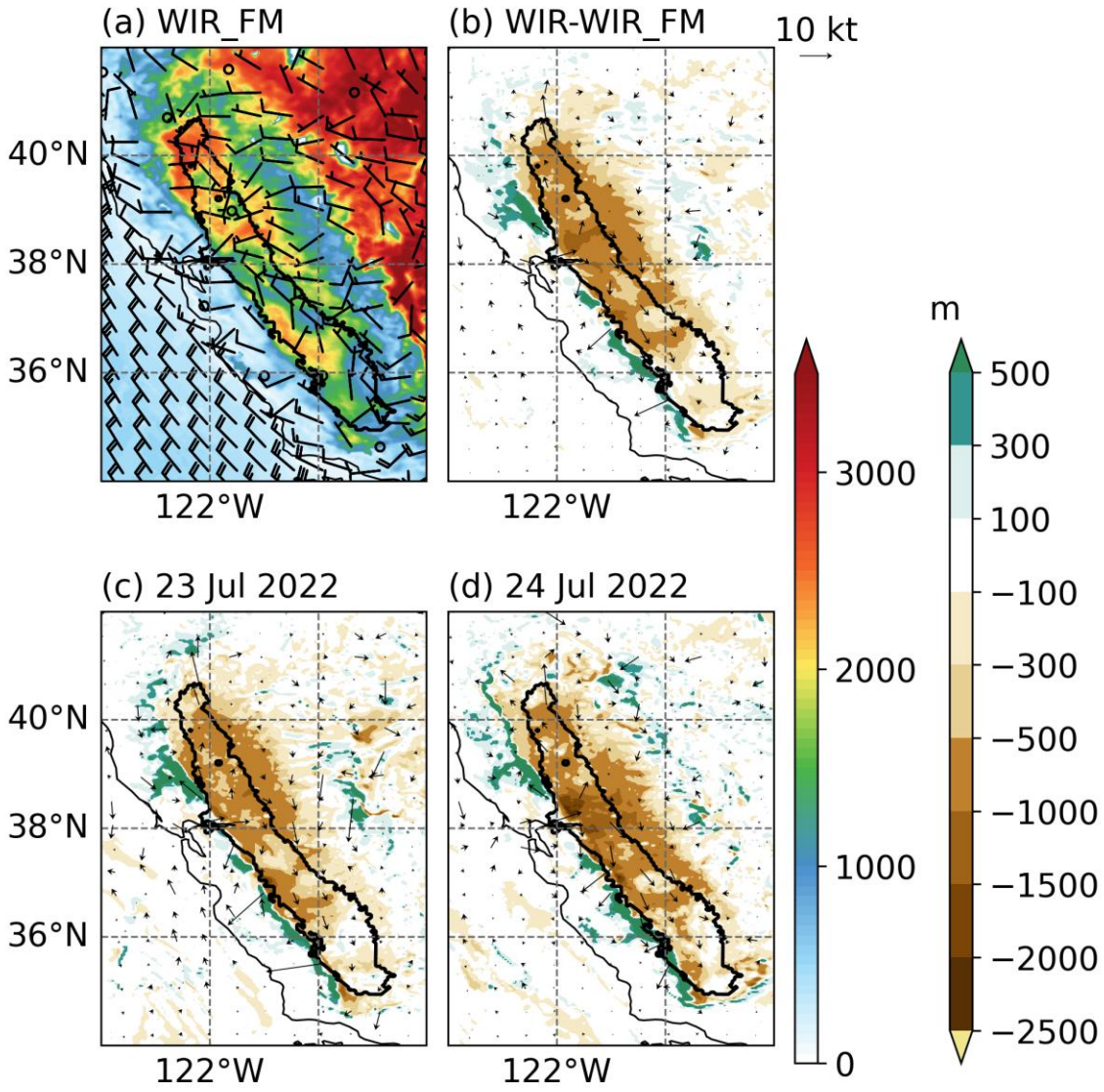


Fig. 10 (a) Average PBLH and the 4th model-level wind at 1500–1700 LT (a) from WIR_FM, and their differences between WIR and WIR_FM on (b) 23 and 24 (averaged), (c) 23, and (d) 24 July 2022.

3.2.3 Trajectory Analysis

To further understand the sources and characteristics of the MAP air flow patterns and their effects on stabilization, 12-h forward trajectories are utilized. Air parcels are released at different elevations in the lower atmosphere (150, 300 and 450 m a.g.l.) over the Delta region outside the CV on 23 July 2022 at 1400 and 1700 LT, when ocean–land temperature contrasts are high.

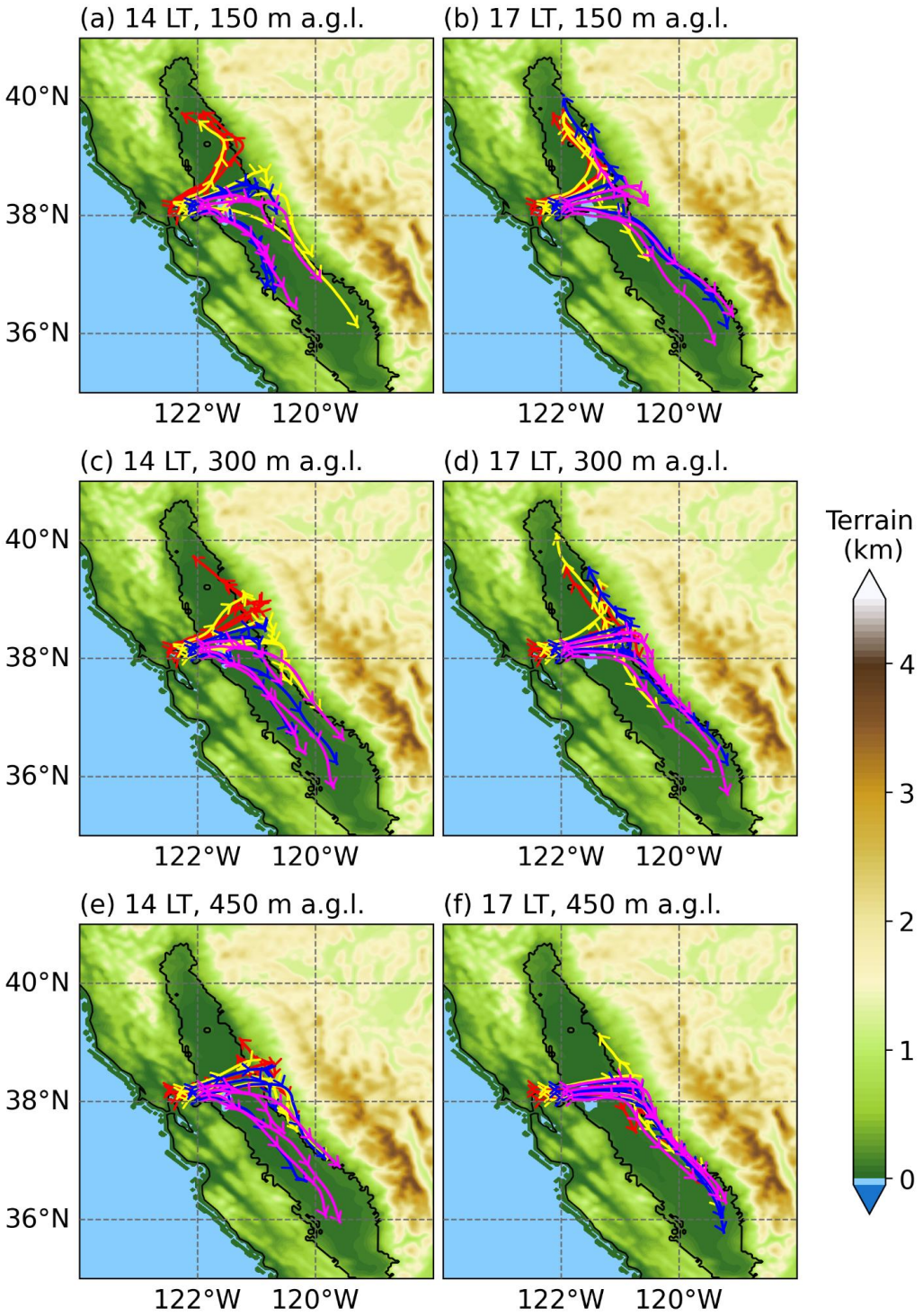


Fig. 11 Twelve-hour forward trajectories, starting at (a, c, e) 1400 LT and (b, d, f) 1700 LT on 23 July 2022, with parcels released near the coast at (a, b) 150 m, (c, d) 300 m and (e, f) 450 m a.g.l. Colours indicate the spatial proximity of the parcel release locations relative to the Delta gap and the open ocean. Red denotes parcels released furthest from the Delta gap and closest to the ocean, transitioning through yellow and blue,

and concluding with magenta for parcels released closest to the Delta gap. The arrows are plotted every three hours from the starting time. The shading shows the terrain.

Parcels released at both times are brought eastward into the central CV, via the Delta gap, by sea breeze. However, unlike the parcels released at 1400 LT or at lower altitudes that travel only to the middle of the CV (Fig. 11a, c, e), those released at 1700 LT or above 300 m a.g.l. tend to travel further south in the southern CV (Fig. 11).

At 150 m a.g.l., more parcels tend to turn north when they are released in the late afternoon (Fig. 11a, b). In contrast, the 450-m parcels all turn toward south regardless of the release time (Fig. 11e, f). These parcel trajectories indicate that in the northern CV, the lower atmosphere is affected by the shallow layer of the cold MAP air, leading to a shallow stabilization layer in WIR (Figs. 4a; 9a). In contrast, a deeper layer of MAP air enters the southern CV, creating a deeper MAP-induced stabilization layer.

In addition, the origins of the air parcels outside the CV affect their MAP pathways. Air parcels released further outside the Delta gap (e.g., close to the ocean; red trajectories in Fig. 11) at 150 m and 300 m a.g.l. are more likely to turn northward after entering the CV, while those released close to the Delta gap (magenta trajectories in Fig. 11) generally turn southward (Figs. 11a–d). On the other hand, parcels released in the southern part of the gap tend to turn southward, and vice versa (Figs. 11a–d).

Overall, the air-parcel forward trajectory analysis provides a broad view of MAP pathways through the Delta gap and highlights their effects on the different stabilization layers in the northern and southern CV.

3.3 The Comparison of Irrigation and MAP Effects

Irrigation and MAP both show cooling effects on T_2 during the day (Figs. 3a; 6a), but their cooling mechanisms are different. Irrigation cools the lower atmosphere by reducing the sensible heat flux, leading to localized cooling effect mainly at irrigation regions (Fig. 3a). In contrast, MAP cooling effect relies on temperature advection, so not only the CV, but also part of the Sierra Nevada are influenced by its cooling effect as well as the PBLH reduction (Figs. 6a; 7).

Irrigation and MAP have opposite effects at night (Figs. 3b; 6b). At night, irrigation warms T_2 due to increased upward ground energy flux from soil to atmosphere that destabilizes the lower atmosphere, while MAP cools T_2 (Fig. 6b) and stabilize the lower

atmosphere. The combined effects on T_2 vary across locations, depending on the spatial distribution of soil moisture and the distance to the MAP source.

Since irrigation and MAP have opposite effects at night but same effects during daytime, we also include the PBLH from WoIR_FM (see Table 1) for comparison in Fig. 9. It is noticed that 1) PBLHs from both WoIR and WoIR_FM peak at 1700–1800 LT, which is 1–2 hours later than from WIR and WIR_FM, implying that irrigation shifts the PBLH peak 1-2 hours earlier, and 2) PBLH from WoIR_FM is the lowest at night among the four experiments, but its PBLH develops the fastest at 0700–0800 LT once solar heating starts (i.e., both MAP and irrigation slow the PBL development in the morning) and becomes the highest among all PBLHs till sunset.

To quantify the contribution of irrigation versus MAP effect on PBLH change, we calculated the PBLH percentage change by each effect (i.e., WIR - WoIR versus WIR - WIR_FM) with respect to the PBLH change by both effects together (i.e., WIR - WoIR_FM; Fig. 12a). Since the percentage change is very sensitive to small PBLH changes in the denominator, only when the PBLH change in WIR - WoIR_FM is greater than 200 m, the percentage is calculated; otherwise, the percentage value is set to invalid (gray shading in Figs. 12b-d).

In the northern CV, irrigation contributes over 50% of the total PBLH reduction, with the largest contribution (70–90%) in the northwestern part of the CV (Fig. 12b), whereas MAP contributes 10–90% of the total PBLH reduction, with the largest contribution near the Delta region and the contribution decreasing as it goes north (Fig. 12c). In the southern CV, irrigation contributes to more than 50% of the total PBLH reduction, with two maximum contributions near 36.5°N, 120°W and near Bakersfield (Fig. 12b). In contrast, the MAP contributes 10–50% of PBLH reduction between 37.5°N and 36.5°N (Nor-SCV), and 0–30% of PBLH reduction south of 36.5°N (Sou-SCV; Fig. 12c). In the central CV, irrigation has a small contribution to PBLH reduction (0–30%) (Fig. 12b), whereas MAP contributes to ~100% of the PBLH reduction, with the maximum at 38.5°N (Fig. 12c). Interestingly, MAP contributes to ~80% of the total PBLH reduction in the northern tip of the CV, which might be explained by the relatively small denominator (0.3–0.5 km) and the mountain wind advection in WIR_FM (Fig. 8b, d). To summarize, the reduction of the PBLH at 1500–1700 LT by the irrigation effect is larger than the MAP effect in both

northern and southern CV, while the MAP effect outweighs the irrigation effect in the central CV.

Figure 12d shows the summation of the percentage contributions from the individual irrigation and MAP effects. If the summation is close to 100%, it implies that the effects of these two processes are quite independent of each other. The result shows that the irrigation and the MAP effects are, in general, independent of each other in the CV, as the summation of Fig. 12b and Fig. 12c is close to 100% over most of the CV, except for the western foothills and the middle part of the Nor-SCV.

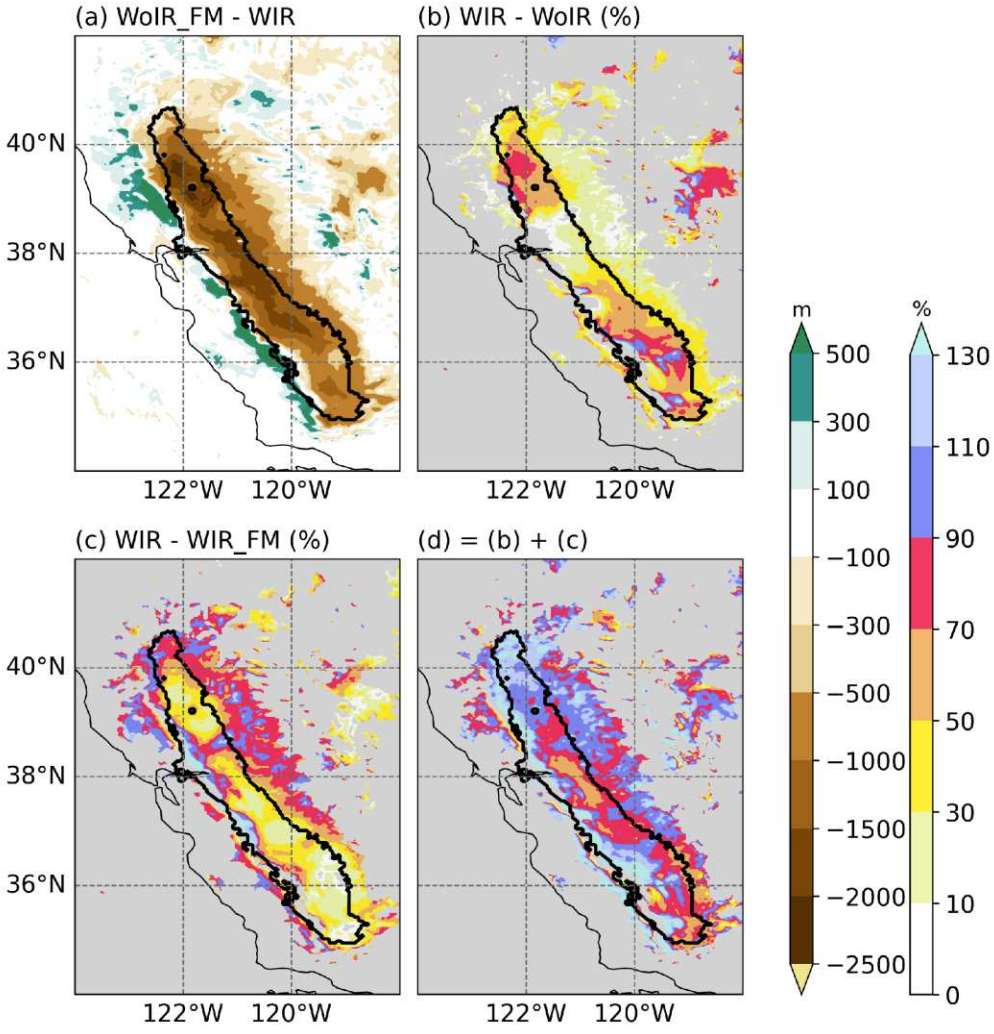


Fig. 12 (a) Average PBLH difference between WoIR_FM and WIR during 23–24 July 2022. The contributions (%) of (b) the irrigation effect (WIR - WoIR) and (c) the MAP effect (WIR - WIR_FM) to the PBLH changes in (a). (d) shows the summation of (b) and (c). Gray colour indicates the areas where PBLH change by the irritation and MAP effects smaller than 200 m.

4 Summary

Summertime PBLH across the CV is influenced by agricultural irrigation and MAP. Previous studies have examined these effects separately, but the individual influences on PBLH were not compared. In addition, to the best of our knowledge, no numerical study has been conducted to assess the MAP effect on summertime PBLH. Unlike earlier work, this study quantifies and compares the impacts of irrigation and MAP influences on PBLH across the CV and investigates the underlying mechanism using the WRF model.

To quantify both effects, four experiments are conducted with the combinations of with (WIR) and without (WoIR) agricultural irrigation, and with and without MAP (WoIR_FM and WIR_FM). To remove the MAP effect, MAP pathways, including the Sacramento-San Joaquin Delta and the Pacheco Pass (near 37°N, 121°W), are blocked by raising the coastal ridge line to a minimum of 700 m.

Model evaluation shows that including irrigation improves the model representation of soil moisture, soil temperature, near-surface meteorology, and PBLH, particularly in the northern CV. Compared to WoIR, PBLHs are reduced in WIR, and the values are closer to observations at the four CARB sites. The daytime PBLH reduction by irrigation corresponds to weaker dry convective mixing, attributed to increased evapotranspiration, which reduces sensible heat flux. In contrast, irrigation warms the lower atmosphere at night because the upward ground energy flux is stronger in WIR than in WoIR.

Irrigation reduces PBLH by 0.5–1.5 km (50–90% of the total PBLH change in WoIR_FM - WIR) in the northern CV, with the largest reduction near Willows (39.5°N, 122°W). The PBLH reduction contributed by irrigation is 0.5–1 km (50–100% of the PBLH change in WoIR_FM - WIR) in most of the southern CV with two maximums at 36.5°N, 120°W and near Bakersfield. Irrigation makes a minimal contribution to PBLH reduction in the central CV, which is mainly driven by MAP.

The MAP cooling effect stabilizes the lower atmosphere day and night, particularly near the Delta region, where T_2 decreases by more than 5°C. This strong stability, contributed by low-level advective cooling, suppresses PBL development. It is noteworthy that the near-surface destabilized layer in WIR, compared to WIR_FM, at night is attributed to enhanced upward sensible heat flux by advecting cold marine air over the warmer surface in WIR.

The MAP-flow, which stabilizes the lower atmosphere and thus reduces PBLH, shows distinct spatial and temporal patterns across the CV. The northern branch of the MAP-flow is shallower (e.g., less than 200 m depth) and more variable (e.g., very strong night-time southerly winds but calm during the day), while the southern branch is deeper (e.g., up to 1 km depth) and more persistent (e.g., strong northerly winds at both day and night).

The MAP-induced reduction in PBLH is widespread across the northern CV and Nor-SCV, with decreases of roughly 0.5–1 km over most of the region, corresponding to the widespread cooling and moistening effects shown in Fig. 6. Despite similar PBLH reductions across the CV, the contribution of MAP reaches 100% of the total PBLH change in the central CV, and the contribution percentage decreases away from the Delta region, the primary MAP source. In the southern CV, MAP-induced PBLH reduction is not only contributed by the Delta Sea breeze, but also by the cold air intrusion through Pacheco Pass, the secondary gap. The two MAP pathways together contribute to roughly 0.5–1 km PBLH reduction (10–50% of total PBLH reduction) in the Nor-SCV. There's minimal PBLH change by MAP in the Sou-SCV (0–0.5 km; 0–30% of total PBLH reduction).

Overall, the MAP effect surpasses the irrigation effect in the central CV whereas the irrigation effect is stronger than the MAP effect in the northern CV. In the southern CV, the irrigation effect becomes more dominant than the MAP effect as it goes south in the Nor-SCV, whereas the irrigation effect dominates in the Sou-SCV, particularly around 36.5°N, 120°W and near Bakersfield.

The findings in this study contribute to a comprehensive understanding of how agricultural irrigation and MAP modulate PBLH across the CV in California, as revealed by WRF simulations of the underlying mechanisms. However, this study focuses on a 7-day simulation with pronounced diurnal variations influenced by the MAP, without addressing longer-term (e.g., seasonal) PBLH changes. Additionally, to avoid the mountain-wave effects caused by the artificially raised ridge, we selected only two days for analysis, which may introduce uncertainty in quantifying the MAP effect, and may not be able to reveal the importance of daytime MAP effects in the northern CV. Last but not least, the absence of radiosonde observations in the CV prevents direct evaluation of modeled vertical profiles of temperature, moisture, winds, and PBLH. Regular radiosonde launches in the CV, particularly at Willows, which is affected by both MAP and irrigation,

would be highly valuable for improving model verification and advancing understanding of local processes.

Acknowledgements This research was supported by the California Air Resources Board (22IT-AQP003). The authors gratefully acknowledge Dr. Kyaw Tha Paw U and Dr. Ian Faloona for valuable discussions that improved this manuscript.

Funding This research was supported by the California Air Resources Board (22IT-AQP003).

Appendix 1: Data Availability Statement

The soil observation data used in this study were provided by collaborators at the University of California, Davis. These data are not publicly available because they are part of an ongoing research program and subject to data ownership and sharing agreements. The data may be made available to qualified researchers for non-commercial research purposes only and with permission of the data owner. Requests for access should be directed to Dr. Kosana Suvocarev (University of California, Davis).

The ceilometer data used in this study were obtained from the California Air Resources Board (CARB). Access to these data is governed by CARB data sharing policies and may require approval. Interested researchers should contact CARB for information on data access.

ERA5 reanalysis data used in this study, including hourly single-level and pressure-level products, are publicly available from the Copernicus Climate Change Service (C3S) Climate Data Store (CDS). The pressure-level data are available as ERA5 hourly data from 1940 to present (Hersbach et al. 2023a), and the single-level data are available as ERA5 hourly data from 1940 to present (Hersbach et al. 2023b).

Model output and derived products generated during this study are not publicly archived due to their large data volume. The model configuration files, namelists, and scripts used to generate the results are available from the corresponding author. Selected subsets of the

model output necessary to reproduce the figures and analyses may be provided upon reasonable request, subject to data transfer limitations.

Appendix 2: Software Availability Statement

The Weather Research and Forecasting (WRF) model version 4.4.2 (Skamarock et al. 2019) was used in this study and is publicly available from the National Center for Atmospheric Research's (NCAR) public WRF-Model Release page on GitHub (https://github.com/wrf-model/WRF/releases). In this study, the standard Noah land surface model within WRF was modified to include an irrigation parameterization following Yu et al. (2025). The modified model code is not publicly available at this time due to ongoing development and usage agreements but can be made available to researchers with appropriate credentials upon reasonable request to the corresponding author.

References

Ackerman, A. S., Hobbs, P. V., & Toon, O. B. (1995). A Model for Particle Microphysics, Turbulent Mixing, and Radiative Transfer in the Stratocumulus-Topped Marine Boundary Layer and Comparisons with Measurements. *Journal of the Atmospheric Sciences*, *52*(8), 1204–1236. https://doi.org/10.1175/1520-0469(1995)052<1204:AMFPMT>2.0.CO;2

Anthes, R. A. (1978). The Height of the Planetary Boundary Layer and the Production of Circulation in a Sea Breeze Model. *Journal of the Atmospheric Sciences*, *35*(7), 1231–1239. https://doi.org/10.1175/1520-0469(1978)035<1231:THOTPB>2.0.CO;2

Berman, S., Ku, J.-Y., & Rao, S. T. (1999). Spatial and Temporal Variation in the Mixing Depth over the Northeastern United States during the Summer of 1995. *Journal of Applied Meteorology*, *38*(12), 1661–1673. https://doi.org/10.1175/1520-0450(1999)038<1661:SATVIT>2.0.CO;2

Bianco, L., Djalalova, I. V., King, C. W., & Wilczak, J. M. (2011). Diurnal Evolution and Annual Variability of Boundary-Layer Height and Its Correlation to Other Meteorological Variables in California's Central Valley. *Boundary-Layer Meteorology*, *140*(3), 491–511. https://doi.org/10.1007/s10546-011-9622-4

Blay-Carreras, E., Pino, D., Vilà-Guerau De Arellano, J., Van De Boer, A., De Coster, O., Darbieu, C., et al. (2014). Role of the residual layer and large-scale subsidence on the development and evolution of the convective boundary layer. *Atmospheric Chemistry and Physics*, *14*(9), 4515–4530. https://doi.org/10.5194/acp-14-4515-2014

Caputi, D. J., Faloona, I., Trousdell, J., Smoot, J., Falk, N., & Conley, S. (2019). Residual layer ozone, mixing, and the nocturnal jet in California's san Joaquin Valley. *Atmospheric Chemistry and Physics*, *19*(7), 4721–4740. https://doi.org/10.5194/acp-19-4721-2019

Caputi, D. J., Trousdell, J., Mehrotra, S., Conley, S., Alexander, G. A., Oldroyd, H. J., & Faloona, I. (2023). Entrainment Rates and Their Synoptic Dependence on Wind Speed Aloft in California's Central Valley. *Boundary-Layer Meteorology*, *186*(3), 505–532. https://doi.org/10.1007/s10546-022-00770-1

Caicedo, V., Delgado, R., Sakai, R., Knepp, T., Williams, D., Cavender, K., Lefer, B., & Szykman, J. (2020). An Automated Common Algorithm for Planetary Boundary Layer Retrievals Using Aerosol Lidars in Support of the U.S. EPA Photochemical Assessment Monitoring Stations Program. Journal of Atmospheric and Oceanic Technology, 37(10), 1847–1864. https://doi.org/10.1175/JTECH-D-20-0050.1

Faloona, I. C., Chiao, S., Eiserloh, A. J., Alvarez, R. J., Kirgis, G., Langford, A. O., et al. (2020). The California baseline ozone transport study (CABOTS). *Bulletin of the American Meteorological Society*, *101*(4), E427–E445. https://doi.org/10.1175/BAMS-D-18-0302.1

Garratt, J. R. (1994). Review: the atmospheric boundary layer. *Earth-Science Reviews*, *37*(1–2), 89–134. https://doi.org/10.1016/0012-8252(94)90026-4

Han, S., Hao, T., Yang, X., Yang, Y., Luo, Z., Zhang, Y., et al. (2023). Land-sea difference of the planetary boundary layer structure and its influence on PM2.5 — Observation and numerical simulation. *Science of The Total Environment*, *858*, 159881. https://doi.org/10.1016/j.scitotenv.2022.159881

Hersbach, H., Bell, B., Berrisford, P., Biavati, G., Horányi, A., Muñoz Sabater, J., Nicolas, J., Peubey, C., Radu, R., Rozum, I., Schepers, D., Simmons, A., Soci, C., Dee, D., & Thépaut, J.-N. (2023a). *ERA5 hourly data on pressure levels from 1940 to present* [Dataset]. Copernicus Climate Change Service (C3S) Climate Data Store. https://doi.org/10.24381/cds.bd0915c6

Hersbach, H., Bell, B., Berrisford, P., Biavati, G., Horányi, A., Muñoz Sabater, J., Nicolas, J., Peubey, C., Radu, R., Rozum, I., Schepers, D., Simmons, A., Soci, C., Dee, D., & Thépaut, J.-N. (2023b). *ERA5 hourly data on single levels from 1940 to present* [Dataset]. Copernicus Climate Change Service (C3S) Climate Data Store. https://doi.org/10.24381/cds.adbb2d47

Hong, S.-Y., & Lim, J.-O. J. (2006). The WRF single-moment 6-class microphysics scheme (WSM6). *J. Korean Meteorol. Soc.*, *42*, 129–151.

Hong, S.-Y., Noh, Y., & Dudhia, J. (2006). A New Vertical Diffusion Package with an Explicit Treatment of Entrainment Processes. *Monthly Weather Review*, *134*(9), 2318–2341. https://doi.org/10.1175/MWR3199.1

Iacono, M. J., Delamere, J. S., Mlawer, E. J., Shephard, M. W., Clough, S. A., & Collins, W. D. (2008). Radiative forcing by long-lived greenhouse gases: Calculations with the AER radiative transfer models. *Journal of Geophysical Research: Atmospheres*, *113*(D13). https://doi.org/10.1029/2008JD009944

Jackson, B. (2021). Simulating summer mixing heights in California's San Joaquin Valley using the WRF meteorological model with three land surface modules. *Meteorology and Atmospheric Physics*, *133*(3), 925–942. https://doi.org/10.1007/s00703-021-00786-1

Jiménez, P. A., Dudhia, J., González-Rouco, J. F., Navarro, J., Montávez, J. P., & García-Bustamante, E. (2012). A Revised Scheme for the WRF Surface Layer Formulation. *Monthly Weather Review*, *140*(3),

898–918. https://doi.org/10.1175/MWR-D-11-00056.1

Li, B., & Avissar, R. (1994). The Impact of Spatial Variability of Land-Surface Characteristics on Land-Surface Heat Fluxes. *Journal of Climate*, *7*(4), 527–537. https://doi.org/10.1175/1520-0442(1994)007<0527:TIOSVO>2.0.CO;2

Li, J., Mahalov, A., & Hyde, P. (2016). Impacts of agricultural irrigation on ozone concentrations in the Central Valley of California and in the contiguous United States based on WRF-Chem simulations. Agricultural and Forest Meteorology, 221, 34–49. https://doi.org/10.1016/J.AGRFORMET.2016.02.004

Mahrt, L. (2014). Stably Stratified Atmospheric Boundary Layers. *Annual Review of Fluid Mechanics*, *46*(1), 23–45. https://doi.org/10.1146/annurev-fluid-010313-141354

Mahrt, L., & Vickers, D. (2006). Extremely Weak Mixing in Stable Conditions. *Boundary-Layer Meteorology*, *119*(1), 19–39. https://doi.org/10.1007/s10546-005-9017-5

Mayor, S. D. (2011). Observations of seven atmospheric density current fronts in Dixon, California. *Monthly Weather Review*, *139*(5), 1338–1351. https://doi.org/10.1175/2010MWR3374.1

Medeiros, B., Hall, A., & Stevens, B. (2005). What Controls the Mean Depth of the PBL?. Journal of Climate, 18(16), 3157-3172. https://doi.org/10.1175/JCLI3417.1

Pal, S., & Lee, T. R. (2019). Contrasting Air Mass Advection Explains Significant Differences in Boundary Layer Depth Seasonal Cycles Under Onshore Versus Offshore Flows. *Geophysical Research Letters*, *46*(5), 2846–2853. https://doi.org/10.1029/2018GL081699

Pan, K., & Faloona, I. C. (2022). The impacts of wildfires on ozone production and boundary layer dynamics in California's Central Valley. *Atmospheric Chemistry and Physics*, *22*(14), 9681–9702. https://doi.org/10.5194/acp-22-9681-2022

Seaman, N. L., Stauffer, D. R., & Lario-Gibbs, A. M. (1995). A Multiscale Four-Dimensional Data Assimilation System Applied in the San Joaquin Valley during SARMAP. Part I: Modeling Design and Basic Performance Characteristics. *Journal of Applied Meteorology*, *34*(8), 1739–1761. https://doi.org/10.1175/1520-0450(1995)034<1739:AMFDDA>2.0.CO;2

Shapkalijevski M, M., Ouwersloot G, H., Moene F, A., & Vilà-Guerau De Arrellano, J. (2017). Integrating canopy and large-scale effects in the convective boundary-layer dynamics during the CHATS experiment. *Atmospheric Chemistry and Physics*, *17*(3), 1626–1640. https://doi.org/10.5194/acp-17-1623-2017

Skamarock, W. C., Klemp, J. B., Dudhia, J., Gill, D. O., Liu, Z., Berner, J., Wang, W., Powers, J. G., Duda, M. G., Barker, D. M., & Huang, X.-Y. (2019). A description of the Advanced Research WRF Version 4 (NCAR Tech. Note NCAR/TN-556+STR, 145 pp.) [Software]. National Center for Atmospheric Research. https://doi.org/10.5065/1dfh-6p97

Sorooshian, S., AghaKouchak, A., & Li, J. (2014). Influence of irrigation on land hydrological processes over California. *Journal of Geophysical Research: Atmospheres*, *119*(23). https://doi.org/10.1002/2014JD022232

Sorooshian, S., Li, J., Hsu, K., & Gao, X. (2011). How significant is the impact of irrigation on the local hydroclimate in California's Central Valley? Comparison of model results with ground and remote-sensing data. *Journal of Geophysical Research*, *116*(D6), D06102. https://doi.org/10.1029/2010JD014775

Sorooshian, S., Li, J., Hsu, K., & Gao, X. (2012). Influence of irrigation schemes used in regional climate models on evapotranspiration estimation: Results and comparative studies from California's Central Valley agricultural regions. *Journal of Geophysical Research: Atmospheres*, *117*(D6). https://doi.org/10.1029/2011JD016978

Stull, R. B. (2012). *An introduction to boundary layer meteorology* (Vol. 13). Springer Science & Business Media.

Sullivan, P. P., Moeng, C.-H., Stevens, B., Lenschow, D. H., & Mayor, S. D. (1998). Structure of the Entrainment Zone Capping the Convective Atmospheric Boundary Layer. *Journal of the Atmospheric Sciences*, *55*(19), 3042–3064. https://doi.org/10.1175/1520-0469(1998)055<3042:SOTEZC>2.0.CO;2

Trousdell, J. F., Conley, S. A., Post, A., & Faloona, I. C. (2016). Observing entrainment mixing, photochemical ozone production, and regional methane emissions by aircraft using a simple mixed-layer framework. *Atmospheric Chemistry and Physics*, *16*(24), 15433–15450. https://doi.org/10.5194/acp-16-15433-2016

Wang, M., & Ullrich, P. (2018). Marine Air Penetration in California's Central Valley: Meteorological Drivers and the Impact of Climate Change. *Journal of Applied Meteorology and Climatology*, *57*(1), 137–154. https://doi.org/10.1175/JAMC-D-17-0089.1

Wilson, J. W., Foote, G. B., Crook, N. A., Fankhauser, J. C., Wade, C. G., Tuttle, J. D., et al. (1992). The Role of Boundary-Layer Convergence Zones and Horizontal Rolls in the Initiation of Thunderstorms: A Case Study. *Monthly Weather Review*, *120*(9), 1785–1815. https://doi.org/10.1175/1520-0493(1992)120<1785:TROBLC>2.0.CO;2

Yang, Z., Dominguez, F., Zeng, X., Hu, H., Gupta, H., & Yang, B. (2017). Impact of Irrigation over the California Central Valley on Regional Climate. *Journal of Hydrometeorology*, *18*(5), 1341–1357. https://doi.org/10.1175/JHM-D-16-0158.1

Yu, Y., Chen, S.-H., Huang, C.-C., Paw U, K. T., Schmitt, C., Zhao, Z., et al. (2025). A Numerical Study of the Agricultural Irrigation Effects on Summer Soil Moisture and Near-Surface Meteorology in California's Central Valley. *Journal of Hydrometeorology*, *26*(6), 641–659. https://doi.org/10.1175/JHM-D-24-0129.1

Zeng, Y., Xie, Z., & Liu, S. (2017). Seasonal effects of irrigation on land–atmosphere latent heat, sensible heat, and carbon fluxes in semiarid basin. *Earth System Dynamics*, *8*(1), 113–127. https://doi.org/10.5194/esd-8-113-2017

Zhang, C., & Wang, Y. (2017). Projected Future Changes of Tropical Cyclone Activity over the Western North and South Pacific in a 20-km-Mesh Regional Climate Model. *Journal of Climate*, *30*(15), 5923–5941. https://doi.org/10.1175/JCLI-D-16-0597.1

Zhong, S., Whiteman, C. D., & Bian, X. (2004). *Diurnal Evolution of Three-Dimensional Wind and Temperature Structure in California's Central Valley*. Journal of Applied Meteorology, 43(11), 1679-1699. https://doi.org/10.1175/JAM2154.1